

Observed Water- and Light-Limitation Across Global Ecosystems

François Jonard^{1,2}, Andrew F. Feldman^{3,4}, Dan J. Short Gianotti⁵, Dara Entekhabi⁵

⁵ ¹ Earth Observation and Ecosystem Modelling Laboratory, SPHERES Research Unit, Université de Liège (ULiege), 4000 Liège, Belgium

² Agrosphere (IBG-3), Institute of Bio- and Geosciences, Forschungszentrum Jülich GmbH, Jülich, Germany

¹⁰ ³ NASA Postdoctoral Program, NASA Goddard Space Flight Center, Greenbelt, MD, USA

⁴ Biospheric Sciences Laboratory, NASA Goddard Space Flight Center, Greenbelt, MD, USA

¹⁰ ⁵ Parsons Laboratory, Department of Civil and Environmental Engineering, Massachusetts Institute of Technology (MIT), Cambridge, MA, USA

Correspondence to: François Jonard (francois.jonard@uliege.be)

Abstract. With a changing climate, it is becoming increasingly critical to understand vegetation responses to limiting environmental factors. Here, we investigate the spatial and temporal patterns of light and water limitation on photosynthesis using an observational framework. Our study is unique in characterizing the nonlinear relationships between photosynthesis and water and light, acknowledging approximately two regime behavior (no limitation and varying degrees of limitation). It is also unique in using an observational framework instead of using model-derived photosynthesis properties. We combine data from three different satellite sensors, i.e., sun-induced chlorophyll fluorescence (SIF) from TROPOMI, surface soil moisture from SMAP, and vegetation greenness from MODIS. We find both single-regime and two-regime models describe SIF sensitivity to soil moisture and photosynthetically active radiation (PAR) across the globe. The distribution and strength of soil moisture limitation on SIF are mapped in the water-limited environments while the distribution and strength of PAR limitations are mapped in the energy-limited environments. Two-regime behavior is detected in 73% of the cases for water limitation on photosynthesis, while two-regime detection is much lower at 41% for light limitation on photosynthesis. SIF sensitivity to PAR strongly increases along moisture gradients, reflecting mesic vegetation's adaptation to making rapid usage of incoming light availability on the weekly timescales. The transition point detected between the two regimes is connected to soil type and mean annual precipitation for the SIF-soil moisture relationship and for the SIF-PAR relationship. These thresholds have therefore an explicit relation to properties of the landscape, although they may also be related to finer details of the vegetation and soil interactions not resolved by the spatial scales here. The simple functions and thresholds are emergent behaviors capturing the interaction of many processes. The observational thresholds and strength of coupling

Using these satellite remote sensing developments, several studies have analyzed the influence of bio-climatic factors on productivity. Madani et al. (2017) found that reanalysis-derived soil moisture (SM), vapor pressure deficit (VPD), and minimum daily air temperature are significant control factors influencing ecosystem productivity over the globe. They showed that SIF was positively correlated with soil moisture on monthly time-scales in dry biomes (e.g., Sahel), whereas in humid biomes (e.g., Amazonia), SIF was negatively correlated with soil moisture and positively correlated to VPD. While Global Ozone Monitoring Experiment-2 (GOME-2) satellite SIF observations were used as proxy of productivity, environmental factors were derived from model reanalysis data, which may have model-prescribed relationships between one another and with productivity. In addition, factors influencing vegetation growth were limited to temperature and moisture constraints, but other environmental controls such as light limitation were not addressed.

Similarly, Nemani et al. (2003) have analyzed the impact of global climate changes on vegetation productivity using global reanalysis data and a production efficiency model. Their results indicate differential controls of light, water, and temperature on vegetation, but with mainly a reduction of climatic constraints to plant growth during the last two decades of the past century, with significant increase in net primary production over large regions of Earth such as in Amazon rain forests. Walker et al. (2020) review theory and evidence suggesting a substantial increase in global photosynthesis since pre-industrial times driven at least in part by increased atmospheric carbon dioxide concentration leading to increases in plant water use efficiency.

Recently, using Orbiting Carbon Observatory-2 (OCO-2) SIF and Soil Moisture Active and Passive (SMAP) SM satellite observations, Gonsamo et al. (2019) found that SM was often a primary limiting factor to plant growth in drylands and croplands. While based on a low number of concurrent SIF and SM data records, the authors observed positive and stronger SIF-SM relationships in drier and warmer regions. In their study, nonlinear behaviors were not addressed.

Using satellite observations of SIF and climate data sets, Liu et al. (2020) found that SM has a dominant role in determining dryness stress on ecosystem production over most land vegetated areas. However, the study was primarily interested in moisture effects, having investigated the relative role of SM and VPD in limiting ecosystem production. Short Gianotti et al. (2019a) showed that SIF-SM relationships match satellite-derived GPP-SM relationships in both time and space, with little-to-no SIF-SM relationship in the light-limited humid regions of the contiguous United States and increasing response strength with aridity. Water-limited regions showed strong increases in ecosystem-water use efficiency (daily SIF or GPP divided by latent heat flux) during SM dry spells.

90 Studies investigating global drivers of photosynthesis tend to focus on linear relationships between these variables, which potentially neglects nonlinear conditions where photosynthesis is not-limited (Gonsamo et al., 2019; Teubner et al., 2018). For example, the light use efficiency (LUE) model is widely used in Earth system modeling to simulate GPP as a linear function of absorbed light (Monteith, 1972). It is becoming more evident that nonlinear plant function behavior exists, especially depending on soil moisture (under dry and wet moisture states) (Feldman et al., 2018; Short 95 Gianotti et al., 2019a; Bassiouni et al., 2020). Those that evaluate nonlinear relationships do so regionally or globally and do not evaluate on a per-pixel basis (Madani et al., 2017). The global patterns of SIF relationships with water and light across climates and biomes remains under-characterized. Yet, the influence of environmental factors on vegetation productivity (and carbon cycle) has both weather timescale and seasonal timescale (relative timing of warm and wet seasons). Both timescales are important and exist in nature. Ecosystem responses on these different timescales 100 are to date not well understood (Linscheid et al., 2020).

The objective of this study is to evaluate the environmental factors that limit surface water and carbon exchanges over vegetated areas. Specifically, we ask: what are the conditions under which SIF is limited by water and light in space and time? Can we detect first-order nonlinear controls of water and light on photosynthesis as suggested from theory? If so, are there climatic controls on the water and light availability thresholds that divide regimes of SIF nonlinear 105 responses to environmental variables? Here, we use an observation-based framework to evaluate nonlinear relationships between SIF and available water and light. Observations are key to provide benchmark information for parameterizing effects of water-stress or light-limitation on ecosystem productivity in Earth system models. Modeled vegetation products can implicitly or explicitly parameterize the relationships between SIF and water and light that we intend to evaluate. In this observationally driven study, we combine three data streams — sun-induced chlorophyll 110 fluorescence (SIF) from TROPOMI, surface soil moisture from SMAP, and normalized difference vegetation index (NDVI) from MODIS—to globally monitor observational evidence for seasonal water-limitation and light-limitation in plant function.

2 Data

Satellite-based data were collected and analyzed for our main per-pixel approach for a 2.5-year period from April 2018 115 to September 2020 (determined by the concurrently available TROPOMI and SMAP data). Climatology information from decade-long time series were used as auxiliary datasets.

2.1 Global Satellite Data

2.1.1 TROPOMI Solar-Induced Fluorescence

Sun-induced chlorophyll fluorescence (SIF, $\text{mW m}^{-2} \text{ nm}^{-1} \text{ sr}^{-1}$) data are obtained from the TROPOspheric Monitoring Instrument (TROPOMI) aboard the Sentinel-5 Precursor (Köhler et al., 2018). TROPOMI provides optical observations with a spectral resolution of 0.5 nm, a spatial resolution of $7 \times 3.5 \text{ km}^2$ (along track x across track) at nadir, and almost global coverage within 1 day. Sentinel-5 Precursor has an overpass time near 13:30 local solar time. SIF is retrieved in a spectral window ranging from 743 to 758 nm using the method of Köhler et al. (2018). SIF observations with large cloud cover (cloud fraction larger than 0.8) were filtered out as described in Köhler et al. (2015). As a robustness test, we additionally use SIF data from the Global Ozone Monitoring Experiment-2 (GOME-2) instrument aboard the MetOp-A satellite, on the period of April 2015 and March 2019, the longest period for which SMAP and GOME-2 are jointly available (Joiner et al. 2013).

2.1.2 SMAP Soil Moisture

Surface soil moisture (SM, $\text{cm}^3 \text{ cm}^{-3}$) data (top 5 cm) are from the L-band (1.4 GHz) microwave radiometer aboard the NASA Soil Moisture Active/Passive (SMAP) satellite (Entekhabi et al., 2010). Microwave observations from the 6 a.m. descending overpasses were used with a spatial resolution of $36 \times 36 \text{ km}^2$ and a global coverage within 3 days. Retrievals of soil moisture were obtained using the multi-temporal dual channel algorithm (MT-DCA) (Feldman et al., 2021; Konings et al., 2016). The MT-DCA algorithm estimates vegetation attenuation and scattering from an algorithm with temporal regularization. It does not use any information on land-use and ecosystem classifications which would bias the results otherwise. While the microwave measurements are commonly known to reflect the top 5 cm, several lines of evidence suggest SM can viably represent relevant root zone dynamics in most cases. First, under wetter conditions, SMAP SM is known to closely correlate with rootzone dynamics, especially in the upper 50 cm (Short Gianotti et al., 2019b; Akbar et al., 2018b). Under drier conditions, microwave emission depth originates from deeper than 5 cm, down to a meter in some cases depending on soil properties (Njoku and Entekhabi 1996). Furthermore, many plants, especially species in semi-arid grasslands where we mainly evaluate SIF-SM, have rooting distributions skewed to the upper layers (<30cm) with preferential uptake of water in the upper soil layers (Flanagan et al., 1992; Meinzer et al., 1999; Miguez-Macho and Fan, 2021). As such, SMAP, in fact, effectively senses soil layers deeper than 15-25 cm, relevant to global root water uptake especially in water-limited ecosystems (Feldman et al. 2022).

2.1.3 MODIS Normalized Difference Vegetation Index (NDVI)

145 Normalized Difference Vegetation Index (NDVI) data come from the Moderate Resolution Imaging Spectroradiometer (MODIS) instrument aboard the NASA Terra satellite. NDVI data between January 1, 2003 and December 31, 2021 were obtained from the Level 3 MODIS product which is a cloud-free 16-day 0.05 degree dataset (MOD13C1, <https://lpdaac.usgs.gov/products/mod13c1v006/>). We linearly resampled the 0.05° grid to the 36 km EASE2 grid. Then, we linearly interpolated the 16-day NDVI data to daily values to determine growing season start and end dates
150 within each pixel.

2.2 Ancillary Data for Analyses

2.2.1 Mean Annual Precipitation and Soil Type

Annual mean precipitation is obtained by averaging annual means between 2010 and 2020 from the Integrated Multi-satellitE Retrievals for GPM (IMERG) final run product combining data from the Global Precipitation Measurement (GPM) satellite constellation (Huffman et al., 2019). Sand and clay fraction information was also obtained from the SoilGrids250m database (Hengl et al., 2017). These metrics were used to evaluate climate gradients of spatial maps generated in the analysis.

2.2.2 MERRA-2 Downwelling Photosynthetically Active Radiation

Daily and downwelling photosynthetically active radiation (PAR, W m⁻²) data are provided by the NASA Modern-
160 Era Retrospective analysis for Research and Applications, Version 2 (MERRA-2) global reanalysis (GMAO, 2015). The spatial resolution is 0.5° x 0.625°. While PAR is an observation-driven modelled product, it is not expected to have strong relationships with vegetation function prescribed within the model because it is driven mainly by solar seasonality and assimilated atmospheric fields such as cloud cover.

2.3 Spatial and Temporal Aggregations

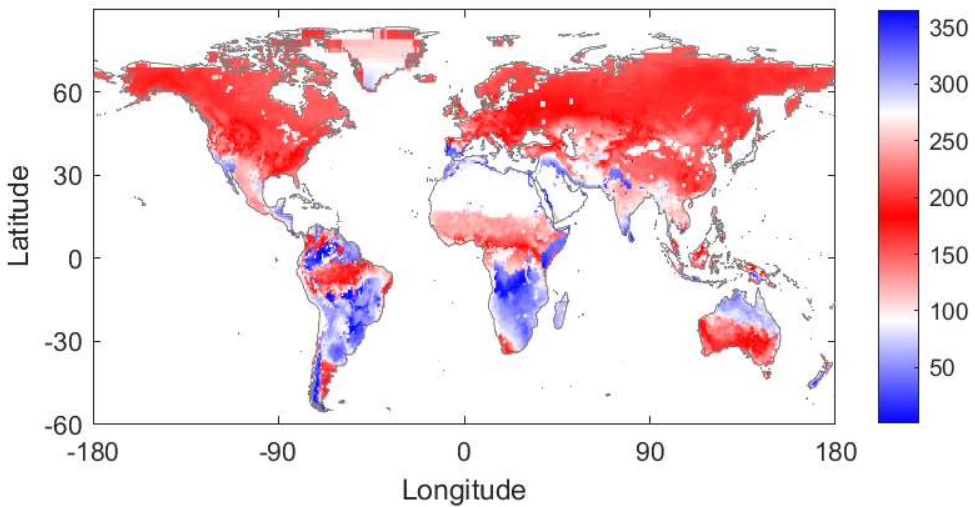
165 The SIF, PAR and NDVI data were regridded on a linear weighting basis to the EASE-2 SMAP grid (36 x 36 km²). The SIF, SM and PAR data were also aggregated temporally to produce 8-day composites. The temporal aggregation was performed to smooth SIF data, with 8-day aggregation selected to match the exact repeat cycle of SMAP. To increase sample size for the correlation maps and the regime classification, the SIF, SM and PAR data at 36 x 36 km² resolution are pooled in 2 x 2 pixel boxes, for each 8-day period. In the following section, all maps have therefore a
170 spatial resolution of 72 x 72 km².

3 Methodology

3.1 Growing Season Estimation

Since we analyze the seasonal water-limitation and light-limitation of plant function only during the growing season, the growing season for each global pixel was first defined using NDVI climatology. The NDVI climatology was 175 developed by averaging 19 years (2003 to 2021) of NDVI data into a mean climatology and smoothing using a 90-day moving average filter (Fig. S1). The growing season was defined by first finding the peak of the NDVI climatology to identify the main growing season and then finding the green up and brown down times as when NDVI reaches its median before and after this peak. This results in growing seasons with a peak on DOY between 100 to 275 in the northern hemisphere and DOY typically 0 to 50 and 300 to 365 in many regions of the southern hemisphere (Fig. 1).

180 There are a number of different approaches to estimating plant phenology based on satellite measurements (e.g. see Bush et al., 2018; Peano et al., 2019; Morellato et al., 2018; Moulin et al., 1997; Zhang et al., 2006). Ultimately the applied technique depends on the application needs, and the approach followed here is sufficient to characterize the active growing season encompassing the primary water and energy interactions with the carbon cycle. It is worth noting that for some regions, several peaks could be observed. The peak with the maximum NDVI was selected corresponding 185 to the “primary growing season”, such as in the tropics, which are characterized by a smaller seasonal amplitude. We additionally tested shorter growing seasons to ensure that shoulder seasons did not influence results.



190
195
Figure 1: Growing season determination based on MODIS satellite normalized difference vegetation index. Day of the year for the phenological peak based on MODIS NDVI climatology. White shading indicates NDVI was not available (bare-soil or water bodies).

200 **3.2 Conceptual Basis**

While chlorophyll fluorescence originates from energy partitioning at the photosystem (leaf) level, SIF presents as an aggregated landscape variable at large spatial and temporal scales (as considered in this study). It is a function of the absorbed PAR ($APAR_{Chl} = PAR \times fPAR_{Chl}$, with $fPAR_{Chl}$ being the fraction of PAR absorbed by chlorophyll pigments and mainly controlled by vegetation cover fraction, LAI, leaf chlorophyll content, and plant structure) and the fluorescence quantum yield (ϕ_F , mainly controlled by leaf biochemical properties and is dependent on plant health and water status), both correlated with photosynthetic productivity and strongly influenced by water and energy (light) availability (Joiner et al., 2014; Jonard et al., 2020; Magney et al., 2020):

$$SIF(\lambda) = PAR \times fPAR_{Chl} \times \phi_F(\lambda) \times f_{esc}(\lambda) \times \tau_{atm}(\lambda), \quad (1)$$

with f_{esc} being the fraction of SIF (at wavelength λ) emitted by the chloroplast that leaves the canopy and τ_{atm} being the fraction of SIF that also passes through the atmosphere (τ_{atm}).

The behavior of the factors in Eq. (1) differ strongly throughout the globe. For instance, annual croplands tend to show large variations in $fPAR_{Chl}$ and f_{esc} during the growing season, while these factors are expected to remain more constant over evergreen forests. The value of ϕ_F is expected to react to the ambient stress conditions. Water- or light limitation comprises the combination of all these components. Light- and water limited photosynthesis will first impact the photosynthetic machinery, affecting ϕ_F . A prolonged water or light limited regime will manifest in primary production and biomass growth, and therefore on $fPAR_{Chl}$ and on f_{esc} . Evaluating the combination of the parameters in Eq. (1) provides insights on the limiting factors of the plant growth. Furthermore, it is expected that many of these parameters are nonlinearly related to water and light limitation (Xu et al., 2021).

We emphasize that it is not our goal to investigate all possible limiting factors on photosynthesis (e.g., temperature, nutrient limitation), nor how they interact to create states where one or both variables is limiting. A more comprehensive analysis can classify states along multiple axes of climatic factors. Our single axes classification provides a first step towards such classifications in detecting globally where, to a first-order, nonlinear relationships between SIF and water and/or light emerge. It also determines observed spatial variations of the types of climatic factor relationships with SIF. The effects of water and light are at least expected to capture the major global limiting pathways based on previous work (Madani et al. 2017).

3.3 Correlation Maps

As a zeroth-order analysis motivating our subsequent evaluation of SIF, we first evaluate the Pearson correlation coefficient between SIF and SM (Fig. 2) and SIF and PAR (Fig. 3) using our 8-day aggregations of each variable. Only values from the growing season are used. In this case, factors that directly limit SIF appear as positively correlated with SIF (in blue in Fig. 2 and 3). Ultimately, the correlation maps guide subsequent analysis of more detailed two-regime behavior. The SIF-SM correlation map (Fig. 2) shows large regions of water limitation (blue regions), such as the Sahel, Eastern and Southern Africa, Eastern Brazil, Southern Asia, and Eastern Australia. The SIF-PAR correlation map (Fig. 3) shows large regions of positive correlation (blue regions), such as much of the United States, Southern Brazil, Europe, and Russia, which are negatively correlated with SM in Fig. 2. Green et al. (2017) provide a more in-depth analysis of linear correspondences between vegetation growth and land/atmosphere variables among others.

Low SIF-SM correlations occur mainly in densely forested regions where soil moisture estimation uncertainty is largest and potentially surface soil moisture is less of a control on vegetation function than other factors. Regions in blue in Fig. 2 are generally in red in Fig. 3, revealing that SM and PAR are typically negatively correlated (Fig. S2). This is due to synoptic-scale correlations between cloud cover and soil moisture (positive) and between cloud cover and shortwave radiation (negative), as well as seasonal-scale alignment of growing-season peaks with peaks in the primarily-limiting component: light or water. Given these considerations, in the remainder of our analysis, we do not evaluate negative relationships between SM (or PAR, separately) and SIF, which could reflect a spurious relationship due to limitation from the other variable. We expect that positive correlations between SM (or PAR) and SIF reflect causal relationships from SM (or PAR) to photosynthesis in limiting environments. We similarly hypothesize that negative correlations between SM and SIF indicate light-limitation or a lagged response of root uptake and increased PAR following precipitation events.

250

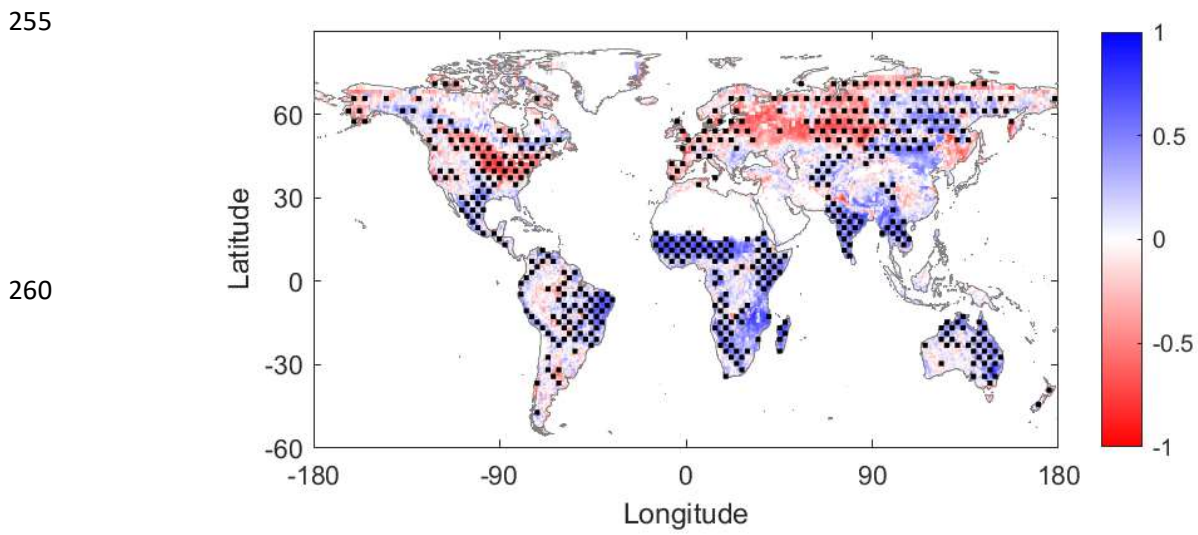


Figure 2: TROPOMI sun-induced chlorophyll fluorescence (SIF) and SMAP MT DCA soil moisture (SM) growing season correlation. Pearson correlation coefficient of 8-day averages. Regions of statistical significance ($P < 0.05$) are indicated with stippling. The stippling corresponds to distributed areas of statistically significant grid points and therefore each statistically significant pixel may not have its own stipple symbol.

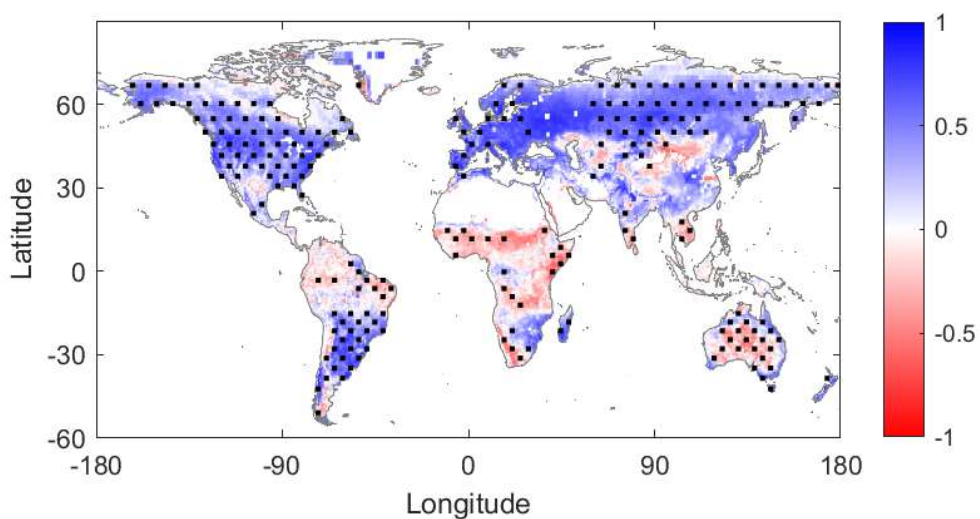


Figure 3: TROPOMI sun-induced chlorophyll fluorescence (SIF) and MERRA-2 photosynthetically active radiation (PAR) growing season correlation. Same conventions as Fig. 2.

3.4 Regime classification

285 Pearson correlation provides information about the degree to which a variable linearly limits SIF. However, in many cases, nonlinear relationships are present where the strength of limitation may decrease above a certain threshold of soil moisture or photosynthetically active radiation (e.g., see Fig. 5). This therefore can bias linear correlations and obscure their interpretation in Figs. 2 and 3 as well as previous studies (Gonsamo et al. 2019). We approximate this relationship here as a two-regime linear model to characterize conditions when water or light limit SIF. In some
290 instances, only one regime may be observed for either water or light. Therefore, three distinct models were tested representing three scenarios for each limitation (water and light) (Fig. 4) as in previous studies that evaluated surface energy fluxes (Akbar et al. 2018a; Feldman et al. 2019).

The following models are used for SM and PAR separately and independently. Only model selections are completed in the pixels where the given variable is positively correlated with SIF (Figs. 2 and 3). If a given pixel shows a positive
295 SIF correlation with both SM and PAR, then models for both SM and PAR are estimated. The first model is the linear model representing the water- or light-limited regime (Fig. 4a and d). Here, the conditions are always characterized by water- or light-limitation without another regime of behavior detected. An increment of SM or PAR always impacts photosynthesis and therefore the SIF. The second model is the full two-regime model representing the two-regimes of water- and light-limitation (Fig. 4b and e). Only when this regime is determined a moisture or light threshold will be
300 estimated. Below this threshold, the given variable limits SIF. Above the threshold, an increment of SM or PAR will not affect photosynthesis. The third model is the zero-slope model for the no water or no light limitation regime (Fig. 4c and f). In this case, plant growth is not sensitive to water or light within the variability observed at that location.

A model is selected based on the Bayesian Information Criterion (BIC) in order to avoid over-fitting among models shown in Fig. 4. Example pixels are shown in Fig. 5 where the two-regime model is selected by this method. Note that
305 we only perform the analysis on pixels with at least 20 pairs of SIF-SM or SIF-PAR.

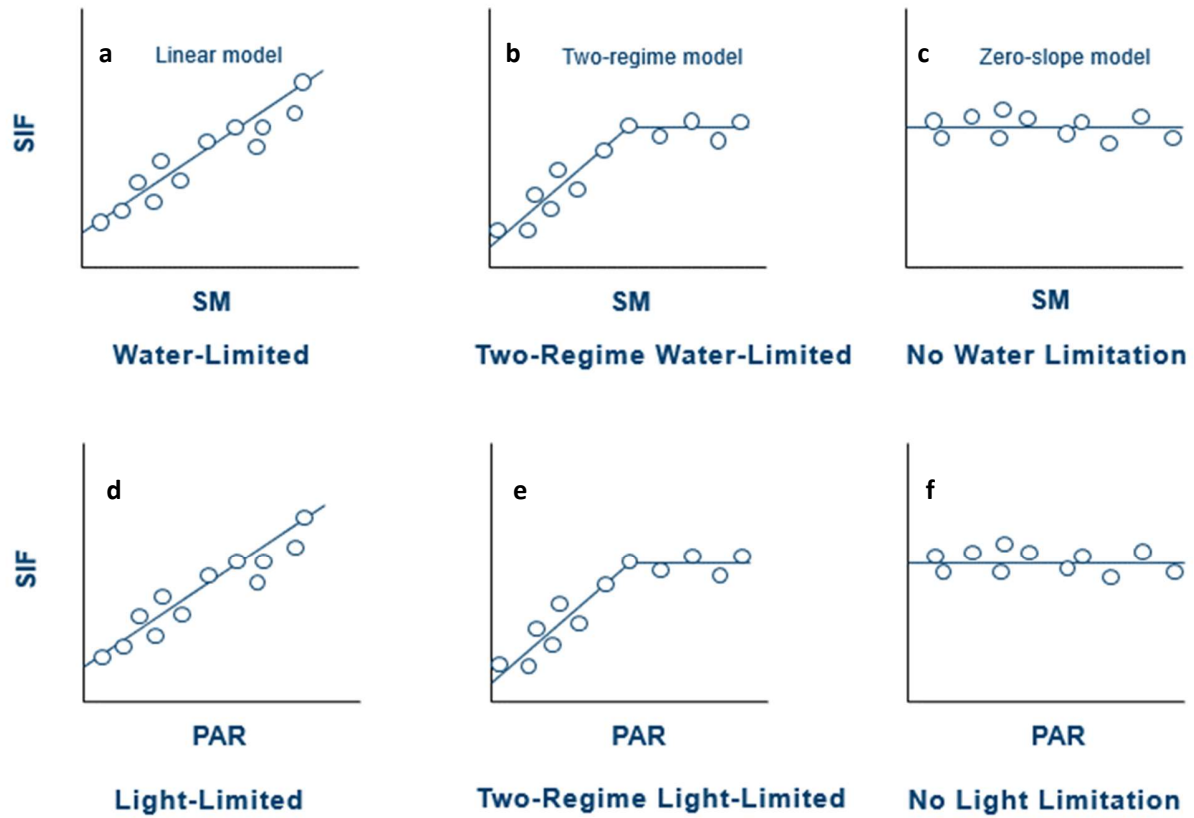
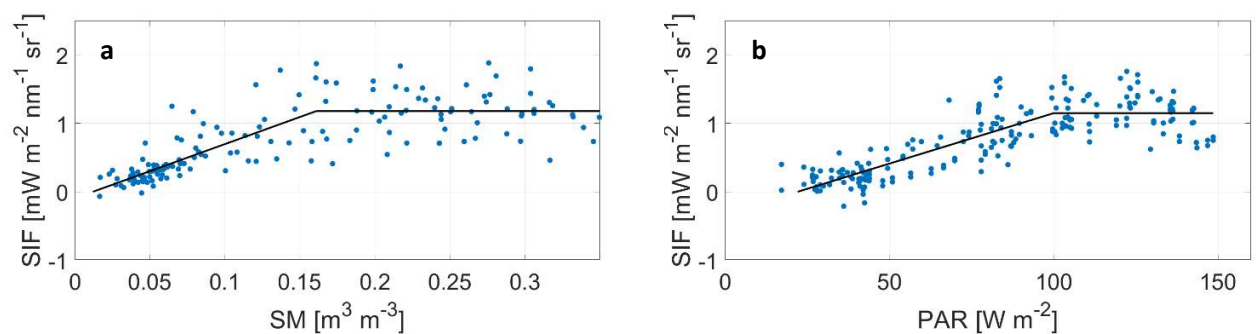


Figure 4: Schematics of model types for the SIF-SM and SIF-PAR regimes. Bayesian Information Criterion (BIC) is used to avoid over-fitting among models during statistical selection.



310

Figure 5: Example SIF relationships with water and light with model estimation from Fig. 4 demonstrated. Scatter plot of (a) sun-induced chlorophyll fluorescence (SIF, $\text{mW m}^{-2} \text{ nm}^{-2} \text{ sr}^{-1}$) and soil moisture (SM, $\text{m}^3 \text{ m}^{-3}$) data and (b) SIF and photosynthetically active radiation (PAR, W m^{-2}) data for the primary growing season and for a single $72 \times 72 \text{ km}^2$ pixel located in (a) Sahel region (Mali) and (b) Spain (Zamora). Data are fitted with a two-regime model.

315 **4 Results and Discussion**

In this section, we present the results of the selection of the best-fit model (based on the Bayesian information criterion) among the three model types described above (linear, two-regime or zero-slope model) for each factor's (water and light) limitation on SIF.

4.1 Water-limited regimes

320 The spatial distribution of the selected model types, the corresponding model slopes, and the frequency distribution of model threshold for the SIF-SM relationship are shown in Fig. 6. Several regions with a two-regime water-limitation can be clearly identified, such as most of sub-Saharan Africa (except the Congo Basin), Southern Asia, Eastern Australia, Eastern Brazil, and Mexico. Few regions are identified as having no water-limitation meaning that while their growing season SIF-SM correlation is positive, it does not aid the fit in model estimation to have a non-zero slope. This likely means that the SIF-SM slope is positive, but near zero. Arid and semi-arid regions, with sparsely vegetated areas, show expected water limitation patterns. Among the pixels showing a water limitation on photosynthesis, 72.5% were characterized by a two-regime behavior, suggesting widespread nonlinearity of the soil moisture controls on vegetation. Therefore, at a given water-limited location, a unit loss of soil moisture typically confers more plant water stress when soil moisture is drier on average than when it is wetter.

330 Slope values are the highest (up to $10 \text{ [mW m}^{-2} \text{ nm}^{-1} \text{ sr}^{-1} \text{]}$ per volumetric water content $[\text{m}^3 \text{ m}^{-3}]$) in the Sahel region, Miombo woodlands south of the Congo Basin (Angola, Zambia, Mozambique), India, the Mekong Basin, and Eastern Brazil. These regions correspond well to the tropical climate, sub-climate savannah, of the Köppen-Geiger climate classification (Beck et al., 2018). In these regions, in the water-limited regime, a small incremental increase of soil moisture corresponds to a large increase in vegetation productivity and therefore the expected 8-day mean fluorescence emission. The high slope values of the regression between SIF and SM in drylands is mainly due to the clear relationship between photosynthetic efficiency, and therefore also ϕ_F , and water availability. As a feedback of the increase in photosynthetic activity, the plant green biomass increases, leading to an increase in $f\text{PAR}_{\text{Chl}}$. The latter effects are especially determined by the water supply over drylands (Moreno-de las Heras et al., 2015). SIF observations allows monitoring of the combined biomass and photosynthetic efficiency effect. Values of the soil moisture threshold are between 0 and $0.45 \text{ m}^3 \text{ m}^{-3}$ with a median around $0.1-0.2 \text{ m}^3 \text{ m}^{-3}$ (Fig. 6c and Fig. S3a for the spatial distribution). When the soil moisture state is above this threshold, SIF has minimal to no water limitation. It is worth noting that the threshold value might be harder to detect for regions with a low slope value. Furthermore, the

SM thresholds are correlated (across space) with soil texture ($\rho = 0.37, P < 0.01$ with clay fraction; $\rho = -0.40, P < 0.01$ with sand fraction). Suchs correlations were similarly observed by Denissen et al. (2020) over Europe. SM thresholds
345 were also broadly assessed based on vegetation types using International Geosphere-Biosphere Program (IGBP) land cover classification information. There is a tendency for the forested and tree covered IGBP classifications to have higher soil moisture thresholds (Fig. S6a), though it is still unclear whether the drivers of the soil moisture threshold are dominated by vegetation characteristics or characteristics of wetter mean climate conditions.

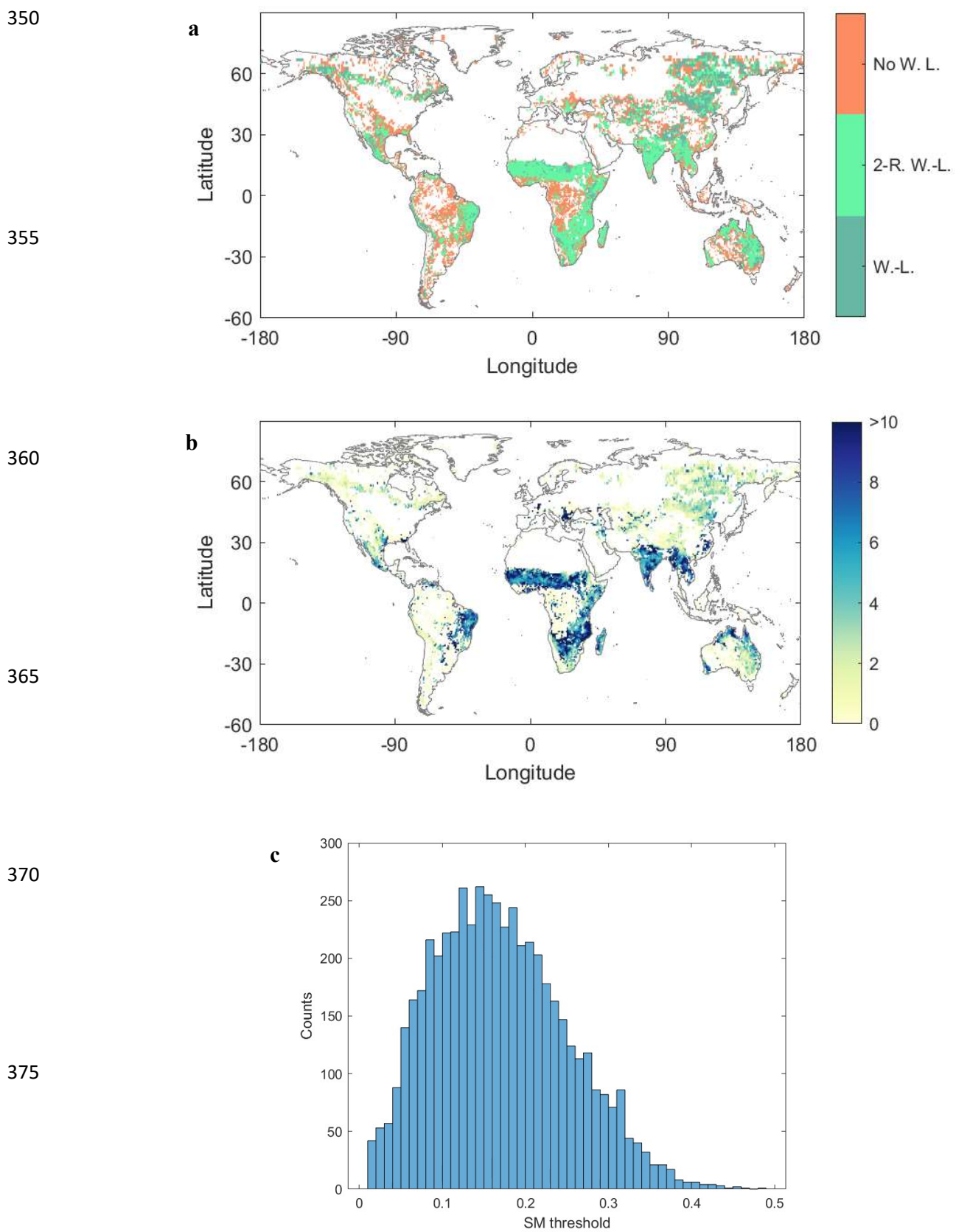


Figure 6: Estimated SIF-soil moisture relationship features. (a) Model type (W.-L.: Water-Limited; 2-R. W.-L.: Two-

380 Regime Water-Limited; No W. L.: No Water Limitation), (b) model slope [$\text{mW m}^{-2} \text{ nm}^{-1} \text{ sr}^{-1}$] in the water-limited regime, and (c) model threshold [$\text{m}^3 \text{ m}^{-3}$] for the SIF-SM relationship. White shading denotes areas where the SIF-SM correlation is not positive—i.e., where SIF is not increasing with SM—or areas where no collocated SIF and SM records are available.

4.2 Light-limited regimes

The spatial distribution of the selected model types, the corresponding model slopes, and the frequency distribution of 385 model threshold for the SIF-PAR relationship are shown in Fig. 7. In contrast to the SIF-SM relationship, a light-limitation regime is observed in many parts of the northern hemisphere, mainly in Southern Canada, the Western U.S., the U.S. East coast, Western and Central Russia, the Balkans, and the Baltic region. Several regions are identified as having a break point between two-regimes of light (non-) limitation, such as Western Europe (France, Spain, Italy, Great-britain), Northern Russia, the U.S. Corn Belt, South-Eastern South America and South-Eastern Africa. Among 390 the pixels showing a light limitation on photosynthesis, only 40.5% were characterized by a two-regime behavior. These regions of two-regime light limitation and threshold behavior is novel given that two-regime light influences on photosynthesis has not been observed or considered at large-scales previously.

Slope values are highest (up to 0.015 [$\text{mW m}^{-2} \text{ nm}^{-1} \text{ sr}^{-1}$] per [W m^{-2}]) in the midlatitudes, specifically in the Great Lakes regions of North America, most of Europe, Southern Russia, Northern Argentina, and Southern Brazil. These 395 regions correspond well to the cold and temperate climates, sub-climate without dry season (hot or warm summer), of the Köppen-Geiger climate classification (Beck et al., 2018). A large proportion of these regions is used for annual crop cultivation. Their green biomass, and therefore the fPAR_{Chl} , is strongly affected by the (cumulative) PAR of the growing season. This explains a large part of the SIF-PAR relationship over these regions. In these regions, a small 400 increment of light will substantially increase the vegetation productivity and therefore the expected fluorescence emission. This suggests that the Calvin cycle of these plants are adapted to strongly respond to light availability compared to other regions. By contrast, in the high latitudes of the northern hemisphere, slope values are the lowest, probably due to lower temperatures and limited seasonal changes in biomass of boreal ecosystems. Values of the estimated PAR threshold are between 0 and 140 [W m^{-2}] with a maximum occurrence around 100-110 [W m^{-2}] (Fig. 7C and Fig. S3b for the spatial distribution). When light availability is above this threshold, SIF has minimal to no 405 light limitation. Such threshold behavior is theoretically expected based on the nonlinear relationship between incoming shortwave radiation and plant carbon fixation (Jones, 2014). Specifically, nonlinear relationships between

SIF and PAR are expected because many plant cellular processes are strongly light-limited in low light environments, but become maximized in brighter environments (Jones, 2014). For example, the light response curve fundamentally defines the rate of leaf-level carbon fixation that is limited under low light environments, but becomes Calvin cycle limited (i.e., carboxylation limiting) in brighter environments where more light marginally produces more carbon uptake (Hermann et al., 2020). Laboratory experiments have shown a decrease in leaf-level fluorescence yield in high light environments (Wang et al., 2018). Similarly, De Cannière et al. (2022) observed a near-linear behaviour of canopy-level SIF emission under low light conditions, while saturating at higher light values. Our threshold and slope estimates here are some of the first large scale observations of these fundamental light-limiting photosynthesis processes.

The PAR thresholds are additionally correlated with soil texture ($\rho = 0.25, P < 0.01$ with clay fraction). We note that PAR may relate strongly with surface temperature at seasonal scales in the northern hemisphere and thus relationships here may include the influence of surface temperature (Buermann et al., 2018; Zhang et al., 2020a). For example, the high SIF slope in the northern hemisphere midlatitudes may be inflated because we do not partition temperature limitation, which requires future investigation.

425

430

435

440

445

450

455

460

465

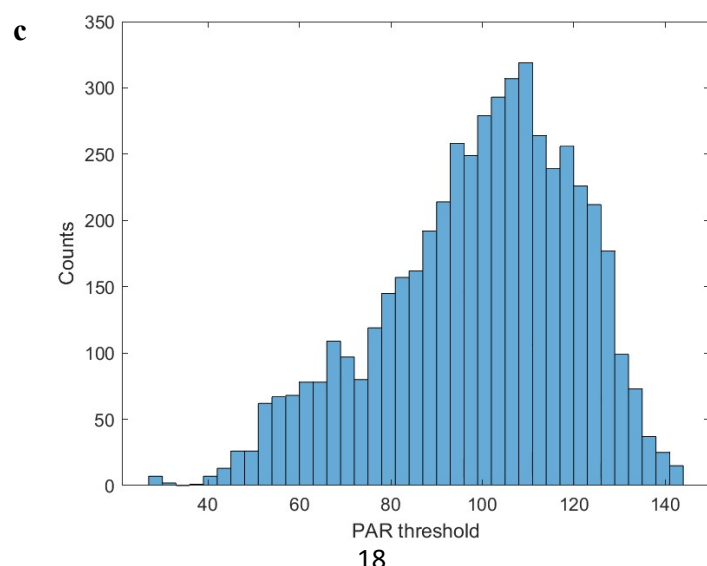
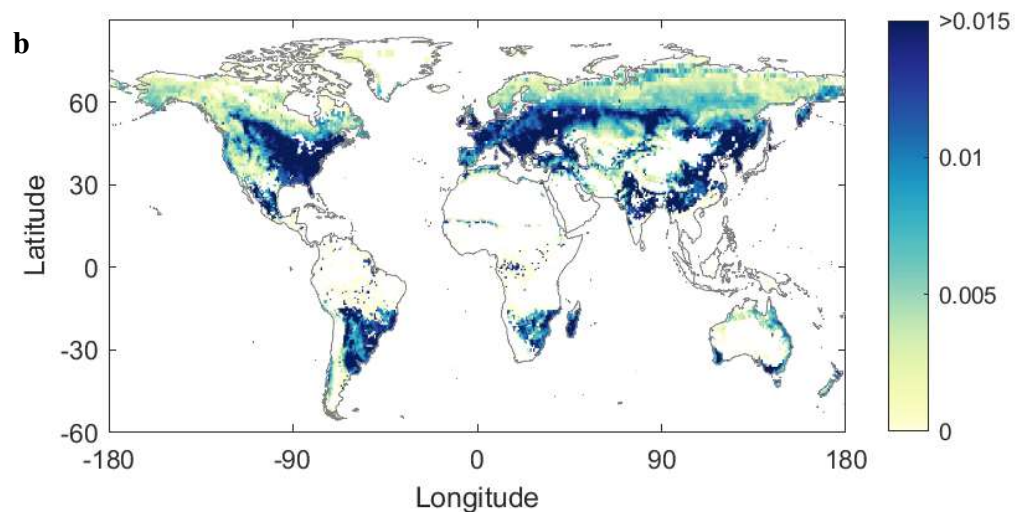
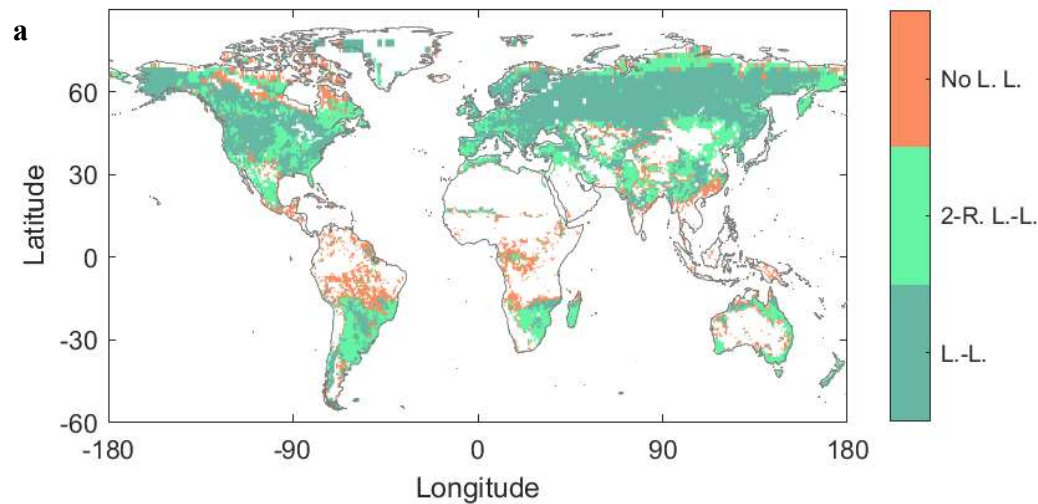


Figure 7: Estimated SIF-photosynthetically active radiation relationship features. Model type (L.-L.: Light-Limited; 2-R. L.-L.: Two-Regime Light-Limited; No W. L.: No Light Limitation), model slope [$10^{-3} \text{ nm}^{-1} \text{ sr}^{-1}$] in the light-limited regime and model threshold [W m^{-2}] for the SIF-PAR relationship. White shading denotes areas where the SIF-PAR correlation is not positive—i.e., where SIF is not increasing with PAR—or areas where no collocated SIF and PAR records are available.

4.3 Relationships of SIF limitation characteristics with mean moisture availability

SIF sensitivity to soil moisture shows a relationship with mean annual precipitation (Fig. 8a; $\rho = 0.32$, $P < 0.01$ with slopes corresponding to sloped part of the two-regime model and the one-regime linear model). Locations with peak slopes occur in the wetter environments such as in India, Southeastern Asia, Angola, and Mozambique. These larger slopes are likely related to the degree to which vegetation responds to mean moisture and individual storms, given the weekly timescales of this analysis (Feldman et al., 2018). It also indicates that these wetter regions may have a stronger plant water stress response when the land surface becomes drier below the soil moisture threshold.

SIF sensitivity to PAR shows an even stronger relationship with annual precipitation (Fig. 8b; $\rho = 0.44$, $P < 0.01$), especially for regions below 1,000 mm yr⁻¹ (Fig. 8b; $R = 0.46$, $P < 0.01$). Sensitivities also peak at approximately 1,000 mm yr⁻¹. The increasing sensitivities may similarly be an adaptation of the vegetation to utilize light availability, given that moisture is typically less limited in these regions.

Furthermore, both SM and PAR thresholds are correlated (across space) with mean annual precipitation (Fig. 8c and d; $\rho = 0.31$ and 0.29, respectively, $P < 0.01$; $\rho = 0.14$ and 0.37, respectively, $P < 0.01$, when considering only regions below 1,000 mm yr⁻¹).

485

490

495

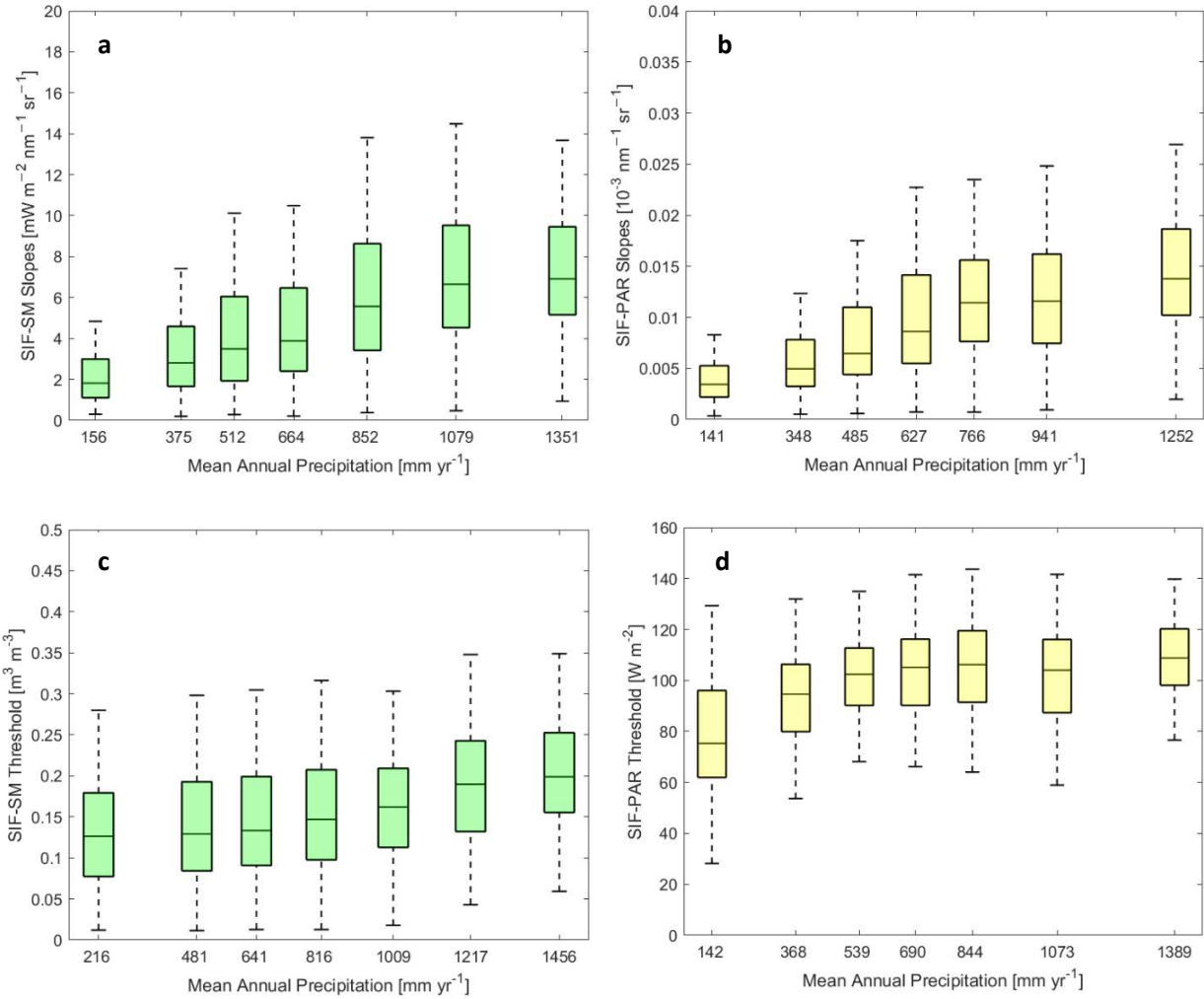


Figure 8: (a) SIF-SM slopes [$\text{mW m}^{-2} \text{nm}^{-1} \text{sr}^{-1}$], (b) SIF-PAR slopes [$10^{-3} \text{nm}^{-1} \text{sr}^{-1}$], (c) SIF-SM threshold [$\text{m}^3 \text{m}^{-3}$] and (d) SIF-PAR thresholds [W m^{-2}] binned as a function of mean annual precipitation [mm yr^{-1}] obtained from the GPM satellite constellation. Slope values correspond to sloped part of the two-regime model and the linear model (see Fig. 4). Each boxplot bin includes the same number of data points (915, 1548, 664 and 629 data points for boxplots (a), (b), (c), and (d), respectively). Box edges are the 25th and 75th percentiles of the distribution bounding the median (red line), and whiskers extend to extrema (maximum and minimum). The median SIF-SM and SIF-PAR slopes and the median SIF-SM and SIF-PAR thresholds all increase with increasing mean annual precipitation.

4.4 Robustness and Limitations

The main sources of uncertainty in this study include: 1) observation errors from the data streams (SIF, SM, PAR), 2) 525 growing season definition errors, 3) model structural and parameter estimation errors, and 4) lack of consideration of all SIF-limiting factors. Here, we discuss each of these error sources and conduct several tests to evaluate the robustness

of results to these errors including repeating the analysis on a different satellite SIF dataset, on alternative growing season definitions and on deseasonalized variables.

To assess the effect of observation errors, we first repeat the analysis with GOME-2 SIF data, which resulted in comparable spatial patterns and thus robustness of the TROPOMI-based results (see Fig. S4). However, the main differences are reduced classification of the regimes with more parameters where the linear and two-regime models are selected less often. This is mainly because GOME-2 SIF results in fewer data pairs which reduces the ability for the model selection to select more parameterized models. TROPOMI was used as the main dataset given that its higher spatiotemporal coverage and lower retrieval noise were essential for the regime classification. We avoid evaluating alternative soil moisture and PAR datasets given that the study would result in a combinatorial analysis which we wish to avoid. Furthermore, it is more appropriate to evaluate alternative SIF measurements because SIF is a weak signal with relatively larger measurement errors given its retrieval from noisy atmospheric properties compared to lower error microwave remote sensing techniques for soil moisture, for example (Jonard et al., 2020; Köhler et al., 2018).

These results are based on a growing season with the start and end defined using the median NDVI (accounting for 540 asymmetrical growing season with dynamic length of about six months). We found that spatial patterns of results were qualitatively the same when repeating the analysis considering a fixed growing season of 3 and 4 months centered on the peak of the NDVI climatology (not shown). Therefore, the results are not a strong function of the growing season definition and are not greatly influenced by transitional time periods before and after the growing season that may be included in our definition. The fact that we condition on the growing season and do not assess the full year removes 545 some influence of seasonality on the results, where too much influence of seasonality may amplify the determined connections between SIF with water and light. We acknowledge that this approach may miss secondary growing seasons in some regions.

Uncertainties from retrieval error can also be evaluated by calculating the coefficient of determination (R^2) and the coefficient of variation (CV) of the model fit as shown in Fig. S5. The R^2 values are generally well above 0.5 in regions 550 where linear and two-regime models are found, and are especially higher in regions with high SIF sensitivity to SM or PAR (higher slopes in Figs. 6b and 7b).

There is potential for structural errors and consequent parameter estimation errors in assuming a piecewise linear model fits a more complex non-linear relationship that has curvature. As such, this creates uncertainties in soil moisture thresholds, for example. Indeed, soil moisture threshold variances determined using the same piecewise linear 555 approaches show robustness of the method with bootstrapped standard deviations less than $0.01 \text{ m}^3/\text{m}^3$ suggesting the

relationship curvature may not bias thresholds greatly (Feldman et al. 2019). Nevertheless, we emphasize the importance of the threshold detection, apart from its numerical value, which occurs despite the presence of curvature. The two-regime model is appropriate given known nonlinear relationships that drive environmental influence on plant function (Jarvis, 1976). As such, studies that do not acknowledge the different regimes and assume linear SIF relationships with the environment would bias estimations of SIF-SM or SIF-PAR relationships. Our results here suggest that with widespread detection of nonlinear SIF relationships with SM and PAR, the commonly used linear correlations and slopes between these variables, ignoring the nonlinearity, will create biases in evaluating water and light limitation. Finally, we repeat the results using AIC rather than BIC to test the selection frequency of the more complex model forms (i.e., linear model and two-regime model). We find that our use of BIC is conservative in 560 selecting more complex models. AIC finds a much more frequent detection of more complex models at a greater risk of overfitting the data over that of BIC (not shown).

Not assessing all limiting variables including temperature and nutrient limitations is a drawback of the analysis. Our analysis indeed misses some limitations on plant function. For instance, no water- and no light-limitation can be seen in the same region (such as tropical forests) where other bio-climatic factors (such as nutrient limitation) could 570 influence plant growth. Predominance of water versus light limiting regime might also shift over the growing season and between years, particularly in transitional climate regions (Seneviratne et al., 2010). However, we also note that the raw SIF-SM relationships, and not their deseasonalized relationships, include coupling from many factors beyond just water-limitation on SIF. We repeat the computation of linear slopes in the limiting regime using deseasonalized variables and find that the relationships are still positive, but are reduced (not shown). Because deseasonalized 575 variables will show a more direct, isolated connection between SIF and each of these limited variables, this analysis indicates that SM and PAR do have direct influences on SIF. However, the higher magnitude slopes in their raw interactions indicate that other factors and their interactions with water and light limitation are included in the SIF-SM and SIF-PAR relationships in addition to the influence of SM and PAR alone. As such, we argue in favor of determining the SIF-SM and SIF-PAR relationships with the raw (non-deseasonalized) variables to assess the state dependence and 580 coupling of multiple limiting factors on SIF. These overall relationships provide a test for model emergent behavior and coupled coevolution of multiple variables and their influence on SIF.

4.5 Future Work

Finally, we aimed to only detect and observe the emerging relationships in nature on how photosynthesis is limited by water and light. The procedure was purposefully naïve and required few assumptions, allowing the observations alone to drive the results. This is a first step in the process of using detection procedures that include interactive effects of water and light with other variables. One can also obtain more mechanistic understanding of physiological behavior by estimating parameters, such as from Eq. (1), from the observed behavior in Figs. 6 and 7. However, these future approaches require more assumptions, which have the added challenge of detecting natural emerging behavior without biasing the results with restrictive assumptions.

The observation-only approach is chosen to best identify the naturally occurring and emerging plant function response to the environment. Such a study informs others that use model or reanalysis frameworks that have built-in assumptions that may confound the results. Nevertheless, the use of PAR from reanalysis here should be updated in the future with globally available shortwave radiation observations. Ultimately, we expect that MERRA-2 PAR is not largely influenced by built-in interactions with land surface behavior given that it is driven mostly by the atmospheric model scheme and assimilation of soundings.

5 Summary and Conclusion

In this study, we map observational evidence for seasonal water-limitation and light-limitation in plant function at the ecosystem scale. We analyzed data from three different satellite sensors, namely sun-induced chlorophyll fluorescence from TROPOMI, surface soil moisture from SMAP, and normalized difference vegetation index from MODIS. In this purely observationally driven study, the combination of the three data streams allowed us to test a set of hypotheses on the types and extent of bio-climatic regions that should be classified as under seasonal water- or light limitation.

To detect where nonlinear controls of water and light on photosynthesis occur, three distinct models were tested representing three scenarios for each limitation (water and light). The first model is the linear model representing the water- or light-limited regime. The second model is the nonlinear two-regime model representing the situation where the rate limitation ceases above a certain threshold of soil moisture or photosynthetically active radiation. The conditions to select this model are conservative and thus we exhibit confidence in the detection of nonlinear controls when this model is selected. The third model is the zero-slope model for the no water or no light limitation regime.

The main results show that soil moisture limits on SIF are found primarily in drier environments while PAR limitations are found in intermediately wet regions. Nonlinear two-regime behavior is observed in 72.5% of the cases for water

610 limitation on photosynthesis, while two-regime detection is much lower at 40.5% for light limitation on photosynthesis. Nevertheless, these nonlinear relationships are theoretically expected and widely observed across the globe for light limitation for the first time here. The widespread nonlinear control of water availability on SIF indicates that dry anomalies will differentially influence plant function: plants are buffered from reductions in water availability when soil moisture is higher, but will strongly respond to unit reduction in water availability under drought conditions. SIF
615 sensitivity to PAR strongly increases along moisture gradients, reflecting mesic vegetation's adaptation to making rapid usage of incoming light availability on the weekly timescales investigated here. The transition point detected between the two regimes is connected to soil type and mean annual precipitation for both the SIF-soil moisture and SIF-PAR relationships. These thresholds have therefore an explicit relation to properties of the landscape, although they may also be related to finer details of the vegetation and soil interactions not resolved by the spatial scales here.
620 Future work can account for interactions between more variables and more explicit characterization of the nonlinear relationships in each pixel. Successful, systematic detection of nonlinear controls of individual environmental variables on photosynthesis with the statistical relationships is a first step here.
While our analysis is not exhaustive in not directly evaluating all possible factors (e.g., vapor pressure deficit, air temperature, nutrients) and their interactions, it highlights that vegetation function exhibits widespread, nonlinear
625 dependencies on bio-climatic factors that are highly spatially variable. Given that we show vegetation existing in limited and non-limiting states depending on the water or light condition, linear correlations of photosynthesis with specific resources provide limited views of landscape-scale photosynthesis. At the same time, many land-surface variables are tightly coupled and thus SM and PAR contain significant information about current meteorological conditions (Feldman et al., 2019). Thus the information captured in bivariate SIF-SM and SIF-PAR relationships
630 represents the real-world coevolution of photosynthesis with these limiting variables as they typically co-evolve with strongly-covarying temperature, VPD, etc.
As such, our study is unique in evaluating (1) the state-dependent, coupled controls on SIF, (2) in detecting the nonlinear relationships between plant function and water and light, major controls on global photosynthesis, and (3) in being an observational framework instead of using model-derived parameters. Our spatial maps therefore can serve
635 as a benchmark to directly validate the model-emergent controls on terrestrial gross primary production from Earth System models.

Acknowledgments

The authors want to acknowledge the Massachusetts Institute of Technology (MIT) for supporting this research with the MIT-Belgium Seed Fund “Early Detection of Plant Water Stress Using Remote Sensing”.

640 References

- Akbar R., Short Gianotti D. J., McColl K. A., Haghghi E., Salvucci G. D., & Entekhabi D. 2018a. Estimation of landscape soil water losses from satellite observations of soil moisture. *Journal of Hydrometeorology*, 19, 871–889.
- Akbar R., Short Gianotti D. S., McColl K. A., Haghghi E., Salvucci G. D., and Entekhabi D. 2018b. Hydrological storage length scales represented by remote sensing estimates of soil moisture and precipitation. *Water Resources Research*, 54, 1476–1492.
- Alemohammad S.H., Fang B., Konings A.G., Aires F., Green J.K., Kolassa J., Miralles D., Prigent C., Gentine P. 2017. Water, Energy, and Carbon with Artificial Neural Networks (WECANN): a statistically based estimate of global surface turbulent fluxes and gross primary productivity using solar-induced fluorescence. *Biogeosciences*, 14, 4101–4124.
- Ahlström A., Raupach M. R., Schurgers G., Smith B., Arneth A., Jung M., Reichstein M., Canadell J. G., Friedlingstein P., Jain A. K., Kato E., Poulter B., Sitch S., Stocker B. D., Viovy N., Wang Y. P., Wiltshire A., Zaehle S., Zeng N. 2015. The dominant role of semi-arid ecosystems in the trend and variability of the land CO₂ sink. *Science*, 348, 895–899.
- Bassiouni M., Good S.P., Still C.J., Higgins C.W. 2020. Plant Water Uptake Thresholds Inferred from Satellite Soil Moisture. *Geophys. Res. Lett.*, e2020GL087077.
- Beck, H., Zimmermann, N., McVicar, T. et al. 2018. Present and future Köppen-Geiger climate classification maps at 1-km resolution. *Scientific Data*, 5, 180214.
- Beer C., Reichstein M., Tomelleri E., Ciais P., Jung M., Carvalhais N., Rödenbeck C., Arain M.A., Baldocchi D., Bonan G.B., Bondeau A., Cescatti A., Lasslop G., Lindroth A., Lomas M., Luyssaert S., Margolis H., Oleson K.W.,

660 Rouspard O., Veenendaal E., Viovy N., Williams C., Woodward F.I., Papale D. 2010. Terrestrial gross carbon dioxide uptake: Global distribution and covariation with climate. *Science*, 329, 834–838.

Buermann W., Forkel M., O’Sullivan M. et al. 2018. Widespread seasonal compensation effects of spring warming on northern plant productivity. *Nature*, 562, 110–114.

665 Bush E.R., Bunnefeld N., Dimoto E., Dikangadissi J.-T., Jeffery K., Tutin C., White L., Abernethy K.A. 2018. Towards effective monitoring of tropical phenology: maximizing returns and reducing uncertainty in long-term studies. *Biotropica*, 50, 455-464.

De Cannière S., Vereecken H., Defourny P., Jonard F. 2022. Remote sensing of instantaneous drought stress at canopy level using sun-induced chlorophyll fluorescence and canopy reflectance. *Remote Sensing*, 14, 2642.

670 Denissen J. M. C., Teuling A. J., Reichstein M., Orth, R. 2020. Critical soil moisture derived from satellite observations over Europe. *Journal of Geophysical Research: Atmospheres*, 125, e2019JD031672.

Entekhabi D. et al. 2010. The Soil Moisture Active Passive (SMAP) mission. *Proc. IEEE*, 98(5), 704-716.

Feldman, A. F., A. G. Konings, M. Piles, D. Entekhabi. 2021. The Multi-Temporal Dual Channel Algorithm (MT-DCA) (Version 4). Zenodo. <https://doi.org/10.5281/zenodo.5579549>

675 Feldman A.F., Short Gianotti D.J., Trigo I.F., Salvucci G.D., Entekhabi D. 2019. Satellite-Based Assessment of Land Surface Energy Partitioning–Soil Moisture Relationships and Effects of Confounding Variables. *Water Resources Research*, 55 (12), 10657-10677.

Feldman A. F., Short Gianotti D. J., Konings A. G., McColl K. A., Akbar R., Salvucci G. D., Entekhabi D. 2018. Moisture pulse-reserve in the soil-plant continuum observed across biomes. *Nature Plants*, 4 (12), 1026-1033.

680 Feldman A.F., Gianotti D. J. S., Dong J., Akbar R., Crow W. T., McColl K. A., Nippert J. B., Tumber-Dávila S. J., Holbrook N. M., Rockwell F. E., Scott R. L., Reichle R. H., Chatterjee A., Joiner J., Poulter B., Entekhabi D. 2022. Satellites capture soil moisture dynamics deeper than a few centimeters and are relevant to plant water uptake. *Earth Sp. Sci. Open Arch.*

- Fisher R.A., Koven C.D., Anderegg W.R.L., Christoffersen B.O., Dietze M.C., Farrior C.E., Holm J.A., Hurt G.C., Knox R.G., Lawrence P.J., Lichstein J.W., Longo M., Matheny A.M., Medvigy D., Muller-Landau H.C., Powell T.L.,
685 Serbin S.P., Sato H., Shuman J.K., Smith B., Trugman A.T., Viskari T., Verbeeck H., Weng E., Xu C., Xu X., Zhang T., Moorcroft P.R. 2018. Vegetation demographics in Earth System Models: A review of progress and priorities. *Glob. Chang. Biol.*, 24, 35–54.
- Flanagan L.B., Ehleringer J.R., Marshall J.D. 1992. Differential uptake of summer precipitation among co-occurring trees and shrubs in a pinyon-juniper woodland. *Plant, Cell Environ.*, 15, 831–836.
- 690 Gentine P., Green J.K., Guérin M., Humphrey V., Seneviratne S.I., Zhang Y., Zhou S. 2019. Coupling between the terrestrial carbon and water cycles—a review. *Environ. Res. Lett.*, 14, 083003.
- Global Modeling and Assimilation Office (GMAO). 2015. MERRA-2 tavg1_2d_lfo_Nx: 2d,1-Hourly,Time-Averaged,Single-Level,Assimilation,Land Surface Forcings V5.12.4, Greenbelt, MD, USA, Goddard Earth Sciences Data and Information Services Center (GES DISC), Accessed: April 15, 2021, 10.5067/L0T5GEG1NYFA
- 695 Gonsamo A., Chen J.M., He L., Sun Y., Rogers C., Liu J. 2019. Exploring SMAP and OCO-2 observations to monitor soil moisture control on photosynthetic activity of global drylands and croplands, *Remote Sensing of Environment*, 232, 111314.
- Green J., Konings A., Alemohammad S. et al. 2017. Regionally strong feedbacks between the atmosphere and terrestrial biosphere. *Nature Geoscience*, 10, 410–414.
- 700 He L., Magney T., Dutta D., Yin Y., Köhler P., Grossmann K., et al. 2020. From the ground to space: Using solar-induced chlorophyll fluorescence to estimate crop productivity. *Geophysical Research Letters*, 47, e2020GL087474.
- Hengl T., Mendes de Jesus J., Heuvelink G. B. M., Ruiperez Gonzalez M., Kilibarda M., Blagotić A., et al. 2017. SoilGrids250m: Global gridded soil information based on machine learning. *PLoS ONE* 12(2): e0169748.
- 705 Huang K., Xia J., Wang Y. et al. 2018. Enhanced peak growth of global vegetation and its key mechanisms. *Nat Ecol Evol*, 2, 1897–1905.

Huffman G., Stocker E.F., Bolvin D.T., Nelkin E.J., Tan, J. 2019. GPM IMERG Final Precipitation L3 Half Hourly 0.1 degree x 0.1 degree V06, Greenbelt, MD, Goddard Earth Sciences Data and Information Services Center (GES DISC), Accessed: 03.01.20.

710 Jarvis P.G. 1976. Interpretation of variations in leaf water potential and stomatal conductance found in canopies in field. *Philos T Roy Soc B*, 273 (927), 593–610.

Jasechko S., Sharp Z.D., Gibson J.J., Birks S.J., Yi Y., Fawcett P.J. 2013. Terrestrial water fluxes dominated by transpiration. *Nature* 496, 347–350.

715 Joiner J., Guanter L., Lindstrom R., Voigt M., Vasilkov A .P., Middleton E. M., Huemmrich K. F., Yoshida Y., Frankenberg C. 2013. Global monitoring of terrestrial chlorophyll fluorescence from moderate-spectral-resolution near-infrared satellite measurements: methodology, simulations, and application to GOME-2. *Atmospheric Measurement Techniques*, 6, 2803-2823.

720 Joiner J., Yoshida Y., Vasilkov A., Schaefer K., Jung M., Guanter L., Zhang Y., Garrity S., Middleton E.M., Huemmrich K.F., Gu L., Marchesini L.B. 2014. The seasonal cycle of satellite chlorophyll fluorescence observations and its relationship to vegetation phenology and ecosystem atmosphere carbon exchange. *Remote Sensing of Environment*, 152, 375-391.

Jonard F., De Cannière S., Brüggemann N., Gentine P., Short Gianotti D. J., Lobet G., Miralles D. J., Montzka C., Pagán B. R., Rascher U., Vereecken H. 2020. Value of chlorophyll fluorescence for quantifying hydrological states and fluxes: Current status and challenges. *Agricultural and Forest Meteorology*, 291, 108088.

725 Jones, H.G., 2014. Plants and Microclimate: A quantitative approach to environmental plant physiology, 3rd ed. Cambridge University Press, Cambridge, UK.

Kerr Y. H. et al. 2010. The SMOS mission: New tool for monitoring key elements of the global water cycle. *Proc. IEEE*, 98(5), 666-687.

- Köhler P, Frankenberg C., Magney T. S., Guanter L., Joiner J., Landgraf J. 2018. Global retrievals of solar-induced chlorophyll fluorescence with TROPOMI: first results and intersensor comparison to OCO-2. *Geophysical Research Letters*, 45 (19), 10456–10463.
- 730 Konings A. G. et al. 2016. Vegetation optical depth and scattering albedo retrieval using time series of dual-polarized L-band radiometer observations. *Remote Sensing of Environment*, 172, 178–189.
- Li W., Migliavacca M., Forkel M., Walther, S., Reichstein M., Orth R. 2021. Revisiting global vegetation controls using multi-layer soil moisture. *Geophysical Research Letters*, 48, e2021GL092856.
- 735 Liang X.-Z., Wu Y., Chambers R.G., Schmoldt D.L., Gao W., Liu C., Liu Y.-A., Sun C., Kennedy J.A. 2017. Determining climate effects on US total agricultural productivity. *Proc. Natl. Acad. Sci.* 114, E2285–E2292.
- Linscheid N., Estupinan-Suarez L. M., Brenning A., Carvalhais N., Cremer F., Gans F., Rammig A., Reichstein M., Sierra C. A., Mahecha M. D. 2020. Towards a global understanding of vegetation–climate dynamics at multiple timescales. *Biogeosciences*, 17, 945–962.
- 740 Liu L., Gudmundsson L., Hauser M., Qin D., Li S., Seneviratne S.I. 2020. Soil moisture dominates dryness stress on ecosystem production globally. *Nat Communication*, 11, 4892.
- Lu X.L., Liu Z.Q., An S.Q., Miralles D.G., Maes W.H., Liu Y.L., Tang J.W. 2018. Potential of solar-induced chlorophyll fluorescence to estimate transpiration in a temperate forest. *Agricultural and Forest Meteorology*, 252, 75.
- Madani N., Kimball J.S., Jones L.A., Parazoo N.C., Guan K. 2017. Global Analysis of Bioclimatic Controls on 745 Ecosystem Productivity Using Satellite Observations of Solar-Induced Chlorophyll Fluorescence. *Remote Sensing*, 9, 530.
- Maes W.H., Pagán B.R., Martens B., Gentile P., Guanter L., Steppe K., Verhoest N.E.C., Dorigo W., Li X., Xiao, J., Miralles D.G. 2020. Sun-induced fluorescence closely linked to ecosystem transpiration as evidenced by satellite data and radiative transfer models. *Remote Sensing of Environment*, 249.
- 750 Maurer G.E., Hallmark A.J., Brown R.F., Sala O.E., Collins S.L. 2020. Sensitivity of primary production to precipitation across the United States. *Ecol. Lett.*, 23, 527–536.

McCarty W., Coy L., Gelaro R., Huang A., Merkova D., Smith E. B., Sienkiewicz M., Wargan K. 2016. MERRA-2 input observations: Summary and initial assessment. Technical Report Series on Global Modeling and Data Assimilation, 46, NASA Tech. Rep. NASA/TM-2016-104606, 61 pp. [Available online at
755 <https://gmao.gsfc.nasa.gov/pubs/docs/McCarty885.pdf>.]

Meinzer F.C., Luis J., Goldstein G., Holbrook N.M., Cavelier J., Wright S.J. 1999. Partitioning of soil water among canopy trees in a seasonally dry tropical forest. *Oecologia*, 293–301.

Miguez-Macho G., Fan Y. 2021. Spatiotemporal origin of soil water taken up by vegetation. *Nature*, 598, 624–628.

Monteith J.L. 1972. Solar Radiation and Productivity in Tropical Ecosystems. *Journal of Applied Ecology*, 9 (3), 747–
760 766.

Morellato L.P.C., Abernethy K., Mendoza I. 2018. Rethinking tropical phenology: insights from long-term monitoring and novel analytical methods. *Biotropica*, 50: 371-373.

Moreno-de las Heras M., Díaz-Sierra R., Turnbull L., Wainwright J. 2015. Assessing vegetation structure and ANPP dynamics in a grassland–shrubland Chihuahuan ecotone using NDVI–rainfall relationships. *Biogeosciences*, 12, 2907-
765 2925

Moulin S., Kergoat L., Viovy N., Dedieu, G. 1997. Global-Scale Assessment of Vegetation Phenology Using NOAA/AVHRR Satellite Measurements. *Journal of Climate*, 10(6), 1154-1170.

Myneni R., Knyazikhin Y., Park T. 2015. MCD15A2H MODIS/Terra+Aqua Leaf Area Index/FPAR 8-day L4 Global 500m SIN Grid V006. NASA EOSDIS Land Processes DAAC. <http://doi.org/10.5067/MODIS/MCD15A2H.006>

770 Nemani R.R., Keeling C.D., Hashimoto H., Jolly W.M., Piper S.C., Tucker C.J., Myneni R.B., Running S.W. 2003. Climate-driven increases in global terrestrial net primary production from 1982 to 1999. *Science*, 300(5625), 1560-1563.

Njoku E.G., Entekhabi, D. 1996. Passive microwave remote sensing of soil moisture. *J. Hydrol.*, 184, 101–129.

- Pagan B.R., Maes W.H., Gentine P., Martens B., Miralles D.G. 2019. Exploring the Potential of Satellite Solar-Induced
775 Fluorescence to Constrain Global Transpiration Estimates. *Remote Sensing*, 11.
- Peano D., Materia S., Collalti A., Alessandri A., Anav A., Bombelli A., Gualdi, S. 2019. Global variability of simulated
and observed vegetation growing season. *Journal of Geophysical Research: Biogeosciences*, 124, 3569-3587.
- Seneviratne S. I., Corti T., Davin E. L., Hirschi M., Jaeger E. B., Lehner I., Orlowsky B., Teuling A. J. 2010.
Investigating soil moisture-climate interactions in a changing climate: A review. *Earth-Sci. Rev.* 99, 125-161.
- 780 Shan N., Ju W.M., Migliavacca M., Martini D., Guanter L., Chen J.M., Goulas Y., Zhang Y.G. 2019. Modeling canopy
conductance and transpiration from solar-induced chlorophyll fluorescence. *Agricultural and Forest Meteorology*, 268,
189-201.
- Short Gianotti D.J., Rigden A.J., Salvucci G.D., Entekhabi D. 2019a. Satellite and Station Observations Demonstrate
Water Availability's Effect on Continental-Scale Evaporative and Photosynthetic Land Surface Dynamics. *Water
785 Resources Research* 55, 540-554.
- Short Gianotti D. J., Salvucci G. D., Akbar R., McColl K. A., Cuenca R., Entekhabi D. 2019b. Landscape water storage
and subsurface correlation from satellite surface soil moisture and precipitation observations. *Water Resources
Research*, 55, 9111– 9132.
- Teubner I.E., Forkel M., Jung M., Liu Y.Y., Miralles D.G., Parinussa R., van der Schalie R., Vreugdenhil M., Schwalm
790 C.R., Tramontana G., Camps-Valls G., Dorigo W.A. 2018. Assessing the relationship between microwave vegetation
optical depth and gross primary production. *Int. J. Appl. Earth Obs. Geoinf.* 65, 79–91.
- Walker A.P. et al. 2020. Integrating the evidence for a terrestrial carbon sink caused by increasing atmospheric CO₂.
New Phytologist, 229: 2413-2445.
- 795 Wang Y., Zheng W., Zheng W. et al. 2018. Physiological and transcriptomic analyses of a yellow-green mutant with
high photosynthetic efficiency in wheat (*Triticum aestivum* L.). *Funct Integr Genomics* 18, 175–194.

- Wang X., Dannenberg M. P., Yan D., Jones M. O., Kimball J. S., Moore D. J. P., et al. 2020. Globally consistent patterns of asynchrony in vegetation phenology derived from optical, microwave, and fluorescence satellite data. *Journal of Geophysical Research: Biogeosciences*, 125, e2020JG005732.
- Xu S., Atherton J., Riikonen A., Zhang C., Oivukkamäki J., MacArthur A., et al. 2021. Structural and photosynthetic dynamics mediate the response of SIF to water stress in a potato crop. *Remote Sensing of Environment*, 263, 112555.
- 800 Zhang X., Friedl M. A., Schaaf, C. B. 2006. Global vegetation phenology from Moderate Resolution Imaging Spectroradiometer (MODIS): Evaluation of global patterns and comparison with in situ measurements. *J. Geophys. Res.*, 111, G04017.
- Zhang Y., Guanter L., Berry J.A., van der Tol C., Yang X., Tang J., Zhang F. 2016. Model-based analysis of the relationship between sun-induced chlorophyll fluorescence and gross primary production for remote sensing applications. *Remote Sensing of Environment*, 187, 145-155.
- 805 Zhang Y., Commane R., Zhou S. et al. 2020a. Light limitation regulates the response of autumn terrestrial carbon uptake to warming. *Nat. Clim. Chang.*, 10, 739–743.
- Zhang Y., Parazoo N. C., Williams A. P., Zhou S., and Gentine P. 2020b. Large and projected strengthening moisture limitation on end-of-season photosynthesis. *Proceedings of the National Academy of Sciences*, 117 (17), 9216-9222.
- 810